Journal of Biomechanics 85 (2019) 6–17

Contents lists available at ScienceDirect

Journal of Biomechanics

journal homepage: www.elsevier.com/locate/jbiomech
www.JBiomech.com

Computational investigation of the Laplace law in compression therapy

Kevork Karakashian [a], Cheryl Pike [b], Raoul van Loon [a,*]

[a] *ZCCE, College of Engineering, Swansea University, United Kingdom*
[b] *Lymphoedema Network Wales, Abertawe Bro-Morgannwg University Health Board, Cimla Health & Social Care Centre, Neath, United Kingdom*

ARTICLE INFO

Article history:
Accepted 12 December 2018

Keywords:
FEA
Lymphedema
Compression garments
Computational modelling
3D camera

ABSTRACT

This study aims to use computational methods for elucidating the effect of limb shape on subgarment and subcutaneous pressures, stresses and strains. A framework was built that generates computational models from 3D arm scans using a depth sensing camera. Finite Element Analysis (FEA) was performed on the scans taken from 23 lymphoedema patients. Subgarment pressures were calculated based on local curvature for each patient and showed a large variability of pressure across each arm. Across the cohort an average maximum subgarment pressure of 5100 Pa was found as opposed to an intended garment pressure of 2500 Pa. Subcutaneous results show that stresses/strains in the adipose tissues more closely follow the subgarment pressures than in the stiffer skin tissues. Another novel finding was that a negative axial gradient in subgarment pressure (from wrist to elbow) consistently led to positive axial gradients for the Von Mises stresses in the adipose tissues; a phenomenon caused by a combination of arm shape and the stiffness ratio between skin and adipose tissues. In conclusion, this work fills a knowledge gap in compression therapy in clinical practice and can inform garment design or lead to optimal treatment strategies.

1. Background

The lymphatic system is responsible for ensuring homeostasis of interstitial tissue fluid and plays a vital role in the immune system (Lawenda et al., 2009). Any impairment to the flow of lymph, which is composed mainly of interstitial fluid, will result in lymphoedema. Consequently, lymphoedema is the accumulation of tissue fluid when the lymphatic system is incapable of sustaining this natural homeostasis (Mortimer and Levick, 2004). As lymphoedema progresses in morbidity, the physiology of the affected region changes. Lymphangions are obliterated, whilst tissue swelling and fibrosis take place along with muscle atrophy and increased fatty tissue (Olszewski et al., 2009). Lymphangions first enter a dilated stage, then a contracted stage and finally a fibrotic stage where they loose their ability to contract (Brennan and Miller, 1998).

Managing patients' symptoms is of great importance due to the immedicable nature of lymphoedema. The affected region can be subjected to various treatments including skin care and massage (manual lymphatic drainage-MLD), along with bandaging and compression garments (Huang et al., 2013). These forms of external pressure and maintenance can be amalgamated to offer best reduction and management of lymphoedema. The exact underlying mechanisms of compression therapy are unclear (Dubuis et al., 2012), yet it has shown to reduce oedema along with tissue stiffness. Compression has been suggested to facilitate fluid movement down a negative pressure gradient, while also reducing capillary filtration (Partsch et al., 2008; Zaleska et al., 2013). Nonetheless, it is difficult with such applications to predict in-vivo sub-bandage pressures and to establish if the prescribed treatment reaches the required threshold and/or expected subcutaneous pressure for optimal lymph drainage (Palfreyman and Michaels, 2009; Piller, 2012).

Sub-bandage pressures could be measured in-vivo, e.g. using pressure sensors, or indirectly via the mechanical testing of garments on cylinders (Gaied et al., 2006). With such indirect methods, the Laplace Law has been implemented in the design of medical garments (Gaied et al., 2006).

In an effort to model the mechanics of soft tissues, Finite Element Analysis (FEA) is widely employed as a tool to quantitatively or qualitatively analyse the response of biological tissues under various conditions (Frauziols et al., 2015; Freutel et al., 2014). It provides the means to gain a better understanding of what soft tissues "feel" when undergoing certain treatments, such as compression therapy. Studies found in literature have used FEA on simplified geometries composed of two dimensional (2D) models, or 3D models but lacking realistic representation of the biological

---

[*] Corresponding author.
E-mail address: R.vanLoon@swansea.ac.uk (R. van Loon).

https://doi.org/10.1016/j.jbiomech.2018.12.021
0021-9290/© 2018 Elsevier Ltd. All rights reserved.

organ (Iivarinen et al., 2013; Iivarinen et al., 2016; Kaczmarek et al., 2013). Therefore, by integrating both aspects of 3D scanning and computational modelling, the aims of this study were to:

- Investigate the deviation of patient-specific sub-bandage pressures from intended sub-bandage pressures based on the assumption of circularity (modified Laplace law).
- Investigate the correlation between sub-bandage pressures and (sub)cutaneous stresses.

3D cameras have been previously used to demonstrate their value for diagnostics of lymphoedema (Buffa et al., 2015; Karakashian et al., 2017). In this work mechanical models were created from these 3D patient scans and FE simulations of garment compression on the arms were performed to explore the potential of this technology even further.

2. Methods

2.1. Patient selection and image pre-processing

A group of 23 women suffering from mild unilateral lymphoedema in their upper limbs (maximum of 20% volume difference between limbs), who were selected for lymphatico-venous anastomosis (LVA) surgery, were scanned using an ASUS Xtion Pro 3D camera (A.X.Pro3D ASUS, Taiwan) as described in our previous study (Karakashian et al., 2017). Research and development approval for this service evaluation, which included the 3D scanning and analysis, was granted by the Abertawe Bro-Morgannwg University Health Board. The 3D camera in combination with the accompanied RecFusion software produced a triangulation of the arm surface (see Fig. A.9a in Appendix A). The concept of circularity was used to identify the elbow for an automated extraction of the lower arm geometry, and the topology and shape of pre-operative scans were then used to create FE models and simulate the compression of soft tissues undergoing garment therapy. The finite element software FEBio developed at the Musculoskeletal Research Laboratories at the University of Utah was used to perform the simulations.

2.2. Material properties

A Neo-Hookean hyperelastic model (see Appendix A) was used to represent the soft tissues as this is widely used in literature (Dubuis et al., 2012; Frauziols et al., 2015; Geerligs et al., 2011; Iivarinen et al., 2013; Tran et al., 2007). Reported stiffness values were used (Table 1) as an adequate representation of the biological tissues, as several other studies have used figures in the same order of magnitude (Iivarinen et al., 2011; Pawlaczyk et al., 2013).

Given the time scales in compression therapy, compressibility was assumed with a Poisson's ratio of 0.4 for the static analysis performed here (Iivarinen et al., 2011; Linder-Ganz and Gefen, 2004). It should be noted that this represents the porous solid part of a normally more complex (i.e. biphasic/triphasic and anisotropic) material behaviour. This simplification facilitates the construction of a framework that can provide easy-to-interpret metrics in the clinic and was deemed appropriate for this study, but could be extended to more complex material behaviour if required. Respective skin and adipose layer thicknesses were chosen as 1.6 mm and 3.1 mm (Iivarinen et al., 2013). The presence of muscle tissue was found to play a negligible role as described in the next section.

2.3. Mesh generation and boundary conditions

For the FE simulations, a volumetric mesh was required based on the triangulated surface description exported from the RecFusion software. This was achieved by creating a hexahedral volumetric template mesh that was then radially projected onto the shape of the forearm as illustrated in Fig. 1.

Table 1
Material parameters used in FE simulations. Muscle played a negligible role in the mechanical analysis and was discarded as explained in the 'Boundary Conditions' section.

Tissue	Young's modulus (kPa) (Iivarinen et al., 2013)	Poisson's ratio (Iivarinen et al., 2013)
Skin	1364	0.4
Adipose	1.17	0.4
Muscle	100	0.4

The original form of the Laplace law, describing transmural pressure across spherical surfaces (Pellicer et al., 2000), can be manipulated to calculate sub-bandage pressures, P (Pa), as shown below:

$$P = \frac{T}{R} = T\kappa, \tag{1}$$

where T is tension (N/m) of the garment and R (m) is the radius of curvature (κ, m^{-1}) of the limb. As it is clinically difficult to measure the curvature of human limbs, their cross-sections are approximated as circles (Gaied et al., 2006), for which the curvature is more easily calculated as $\kappa_{circle} = 1/\widehat{R}$, where $\widehat{R}$ is typically the radius approximated from measuring the perimeter (assumed to be $2\pi\widehat{R}$). Such approximation is common with the indirect methods for measuring sub-bandage pressures and is carried out by the modified Laplace law to calculate pressures for bandaging applications (Gaied et al., 2006; Macintyre, 2007).

The Laplace law was employed to calculate the pressure distribution as a boundary condition on the outer skin. For a fair comparison between different arm topologies, all forearms were imposed with the same intended garment pressure, P_g, of 2500 Pa at the wrist, declining linearly to 2250 Pa at the elbow (10% reduction). The pressure 2500 Pa (approx. 18.7 mmHg) is a representative value applied by class 1 upper limb garments (across different standards), having a range between 15 mmHg and 21 mmHg (Krimmel, 2009). The actual pressure distribution, $\widetilde{P}$, depends on the arm shape for each given patient and was prescribed as a Neumann boundary condition. The calculation of $\widetilde{P}$ was performed in two main steps.

1. The required tension $T(\hat{z}_\ell)$ at the ℓ-th cross-section was calculated by rearranging Eq. (1). The pressure term was equated to the intended garment pressure gradient, P_g, and curvature was calculated by assuming the girth, $C(\hat{z}_\ell)$, of each cross-section (based on the scan) to be equal to $2\pi R(\hat{z}_\ell)$, as typically assumed by manufacturers (Gaied et al., 2006; Macintyre, 2007):
   $C(\hat{z}_\ell) = 2\pi R(\hat{z}_\ell) \rightarrow R(\hat{z}_\ell) \rightarrow \kappa_{circle} = \frac{1}{R(\hat{z}_\ell)} \rightarrow T(\hat{z}_\ell) = \frac{P_g}{\kappa_{circle}},$
2. The actual pressure profile, $\widetilde{P}$, was then calculated using the local curvature, $\widetilde{\kappa}\left(\hat{\theta}_j, \hat{z}_\ell\right)$, and previously calculated tension values, $T(\hat{z}_\ell)$:
   $\widetilde{P}\left(\hat{\theta}_j, \hat{z}_\ell\right) = T(\hat{z}_\ell)\widetilde{\kappa}\left(\hat{\theta}_j, \hat{z}_\ell\right).$

The local curvature was calculated using polar coordinates as shown in Eq. (2). $\widetilde{R}'\left(\hat{\theta}_j, \hat{z}_\ell\right)$ and $\widetilde{R}''\left(\hat{\theta}_j, \hat{z}_\ell\right)$ are the first and second order derivatives with respect to θ at each cross-section. Fig. 1d shows the variation of the boundary conditions (pressure) around the cross-section of an elbow. Note that the application of pressure at each cross-section was increased from zero, up to the maximum pressure dictated by $\widetilde{P}\left(\hat{\theta}_j, \hat{z}_\ell\right)$. In each quasi-static step, the

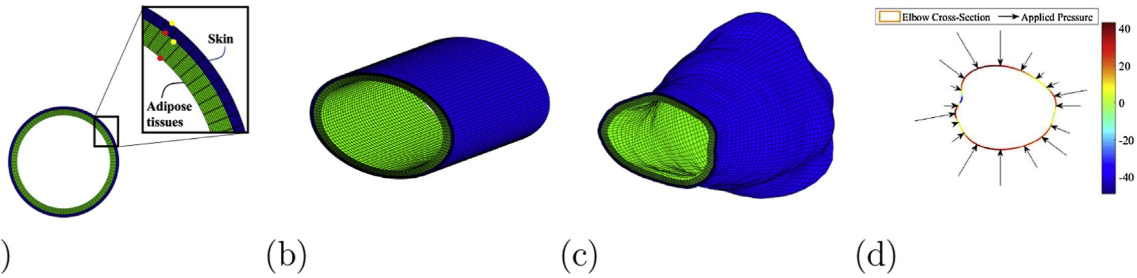

Fig. 1. (a) 2D mesh before extrusion and morphing. The cross-sectional area is composed of skin (blue) and adipose (green) tissues respectively. The red and yellow dot indicate the location of the "inner layers" and "outer layers", respectively. The mechanical contribution of muscle was negligible (Fig. 2). (b) Extrusion of the mesh into a structured hexahedral mesh. (c) 3D morphed template mesh through radial projection onto the 3D scans. The inner geometry was then morphed into the forearm's shape by radially displacing the nodes, either outward or inwards, in MATLAB. Note that the thickness of the soft tissues is maintained during this morphing process. (d) Representation of the pressure distribution across the perimeter at the location of the elbow. The length of the arrows represents the magnitude of pressure applied. The colour code increases from blue, depicting negative curvature (m^{-1}) of concave parts that would not be in contact with the garment, to red, depicting positive curvatures of convex regions. (For interpretation of the references to colour in this figure legend, the reader is referred to the web version of this article.)

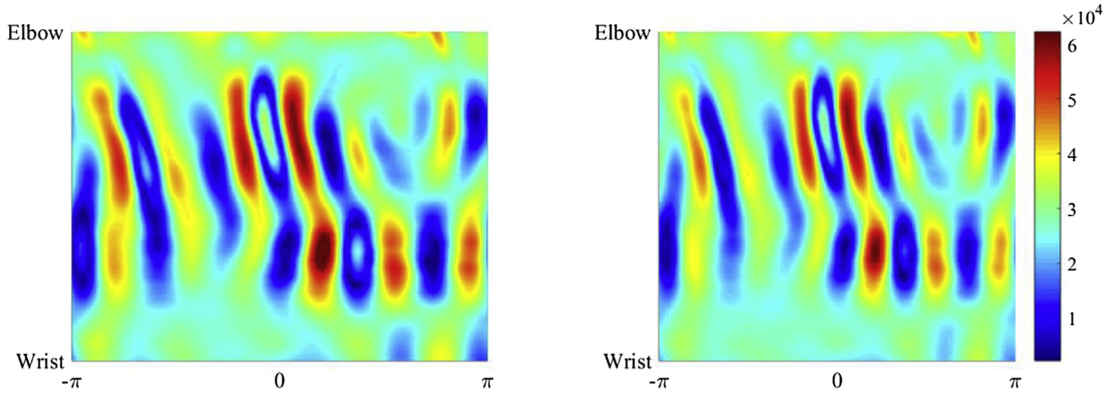

(a) 1 cm muscle thickness (b) Muscle tissue absent

Fig. 2. Varying the thickness of muscle tissue from 1 cm to 0 cm, had a negligible effect on the von Mises stress distributions (Pa) in skin. Similar results were found for the subcutaneous stress distributions.

curvature was updated (depending on the tissue deformations) to emulate the interaction between the compression garment and the skin.

$$\kappa\left(\hat{\theta}_j,\hat{z}_\ell\right) = \frac{R^2\left(\hat{\theta}_j,\hat{z}_\ell\right) + 2R'^2\left(\hat{\theta}_j,\hat{z}_\ell\right) - R\left(\hat{\theta}_j,\hat{z}_\ell\right)R''\left(\hat{\theta}_j,\hat{z}_\ell\right)}{\left(R^2\left(\hat{\theta}_j,\hat{z}_\ell\right) + R'^2\left(\hat{\theta}_j,\hat{z}_\ell\right)\right)^{3/2}} \tag{2}$$

The bottom and top ends of the forearm were fixed axially. The significance of muscle tissue was tested by introducing an additional muscle layer to the geometry shown in Fig. 1 and varying its thickness from 1 cm down to 0 cm. This showed that the muscle layer had little to no effect on the stress/strain distributions in the adipose and skin tissues of the forearms, due to its relatively high stiffness value (Fig. 2). We therefore omitted muscle tissue and prescribed fixed boundary conditions at the adipose-muscle interface instead of muscle-bone interface. A mesh sensitivity analysis was carried out resulting in 8 elements across the skin layer, 12 in adipose, 40 axially and 100 circumferentially.

3. Results

FE simulations were carried out on the oedematous forearms of all 23 patients. The results are detailed in three main sections. First, the use of Laplace Law was analysed, especially due to the variation of topology between different patients. Second, the variation in (sub)cutaneous stress and strain distributions were studied. Finally, material parameters were varied to emulate the changes in physiology with the progression of lymphoedema. Stress and strain distributions were analysed along three main regions; outer layer of skin, and the first and final layers of adipose tissue. (Note: Against engineering convention all positive stresses presented in this paper are compressive).

3.1. Delivered pressures and Laplace law

As garments are used extensively to treat lymphoedema, it is of great value to compare the applied pressure ($\widetilde{P}$) subject to the non-circularity, and the intended pressure (P_g) based on the assumption of circularity. Fig. 3 shows the variation of pressure across a randomly chosen forearm (patient 21). The actual delivered pressure ranges from zero (at positions of negative circularity) to more than twice the maximum applied pressure at the wrist. In fact, the maximum delivered pressure across the cohort had an average of 5100 Pa. These high peaks do not necessarily occur at the wrist, where the maximum pressure ($P_g(z_{wrist})$) was intended, owing to the large changes in curvature across the arm. It should be noted that these values are the variation of the applied pressure, $\widetilde{P}$, which is determined by the arm shape, and not by the mechanical (FE)

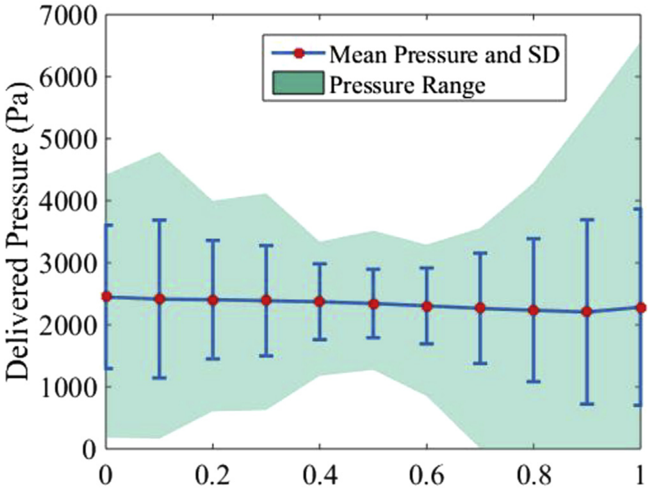

Fig. 3. Delivered pressure along the length of a forearm from wrist (0) to elbow (1). Solid line represents the average pressure delivered and the standard deviation (SD) at each cross-section. The shaded region represents the maximum and minimum pressures at those cross-sections. The actual applied pressure profile decreased from 2500 Pa at the wrist, down to 2250 Pa at the elbow (10% reduction).

analysis. The mean circumferential value of delivered pressure (red[1] dots in Fig. 3) was slightly lower than the intended pressure, P_g, i.e. across the cohort, the average delivered pressure reduced from 2445 Pa at the wrist, down to 2246 Pa at the elbow.

To gain a better appreciation for the difference between the expected pressures and the actual delivered pressures, $\widetilde{P}$, an idealised version of each forearm was created. Each cross-section on the actual forearm was made circular based on the girth/perimeter. The root mean square error (RMSE) between the idealised and actual pressures was calculated for all 23 forearms. On average, the RMSE value was ≈945 Pa.

Carrying out identical FE simulations on both idealised and scan-based geometries allowed a comparison of stress distributions in skin and adipose tissues. Fig. 4 shows the variation of von Mises stress distributions at the outer layer of skin for both types of geometries. As expected, the stress distribution of the idealised forearm is more homogeneous than the scan-based geometry. Average RMSE across the cohort, between idealised and actual stress distributions, were 4405 Pa, 89 Pa, and 103 Pa at the outer skin layer, first and final layers of adipose tissue respectively.

3.2. (Sub)cutaneous stress and strain distributions

Results of the simulations show a heterogeneous distribution for stresses and strains as experienced by skin and adipose tissues. The mean stress experienced by the outer skin was on average an order of magnitude higher than the applied pressure profile, and falls two orders of magnitude by the time it reaches the fat-muscle interface. Since the direction of these distributions are inherently affected by the curvature of the outer surface, the correlation (ρ) between curvature, κ, and stress/strain distributions, X, was calculated as:

$$\rho = \frac{\sum_i^{N_\theta}\sum_j^{N_z}\left(\kappa_{ij}-\bar{\kappa}\right)\left(X_{ij}-\overline{X}\right)}{\sqrt{\left(\sum_i^{N_\theta}\sum_j^{N_z}\left(\kappa_{ij}-\bar{\kappa}\right)^2\right)\left(\sum_i^{N_\theta}\sum_j^{N_z}\left(X_{ij}-\overline{X}\right)^2\right)}}, \tag{3}$$

where $\bar{\kappa}$ and $\overline{X}$ are the mean values for each metric. The average correlation across the cohort between stresses and curvature was 0.1275 at the outer layer of skin, 0.4225 at outer layer of adipose tissue, and 0.4070 at the inner of adipose tissue. Similar values were found for strain. This correlation could be visually inspected as shown in Fig. 4. Note how high strains/stresses do not only occur in convex regions, but also in concave (negative curvature) regions.

Fig. 5 summarises the variation of skin and adipose stresses for all patients. To compare the same anatomical positions across the cohort, stress values were taken from the wrist to the elbow at 11 equispaced points.

The stresses calculated in both modelled tissues do not follow the intended negative axial pressure gradient (Fig. 5). In fact, stresses in the skin showed a positive axial gradient for most patients, i.e. low Von Mises stresses at the wrist, whilst higher at the elbow (Fig. 5c). In the adipose tissue these trends were even stronger with a consistent positive Von Mises stress gradient across all forearms (Fig. 5d and 4e). These unexpected positive gradients were consistent with analytical findings using elastic thick-walled compound cylinder theory under plane stress conditions (see Appendix A). Using the circumferential and radial stresses from the analytical formulations, von-Mises stress distributions were calculated for a two-layered (skin and fat) tapered cylinder. Fig. 6 demonstrates the unexpected increase in the von Mises stresses across the cylinder. Von Mises stresses were noticeably proportional to the circumferential stress component, especially in skin. As expected, both tissues moved inwards, yet not by the same amount. It was observed that the outer layer of skin tissue displaced less than the inner layer of skin, which means that the skin tissue thickens radially. The displacements then decrease from a maximum at the skin-adipose interface down to zero at the fixed boundary conditions. This behaviour was consistent with the FE simulations.

3.3. Sensitivity to material parameters, boundary conditions and tissue thickness

Up to this point, the effect of geometry on stress/strain distributions has been investigated and the choice of consistent material parameters for all subjects seems justified. To account for some of the physiological changes that occur with the progression of lymphoedema, such as fibrosis and increased fatty tissue thickness, the stiffness of the adipose tissue was doubled and quadrupled, whilst its thickness was increased by 35%. Fig. 7 depicts the changes in stresses and strains across the modelled tissues. Stresses are more dominant in the skin tissue, whilst deformations or strains are larger in the adipose tissue. A thicker adipose tissue decreased deformations when comparing the same stiffness values (Fig. 7 green vs blue lines). The transmission of sub-bandage pressures into the subcutaneous tissues was evaluated by calculating the correlation between the 2D maps of curvature and stresses/strains. Increasing the stiffness of the adipose tissue, increased the correlation (ρ) to about 0.5 in the skin, and to 0.7 across the fatty tissue. It also caused the von Mises stresses in skin to follow the applied sub-bandage pressure gradient, i.e. an opposite gradient to what is seen in Fig. 5c. However, this change in direction/-gradient was not observed for the adipose tissue.

A further sensitivity analysis was performed to investigate the effects of:

- Intended pressure gradients.
- Intended pressure magnitude.
- Adipose tissue variability in circumferential direction.

The gradients in circumferential stress reduce with a reducing gradient of P_g for both the skin and the adipose tissues (Fig. 8a and b), whilst the trends caused by local shape features remain the same. In more chronic lymphoedema the tissue becomes more

---

[1] For interpretation of color in Figs. 3 and 7, the reader is referred to the web version of this article.

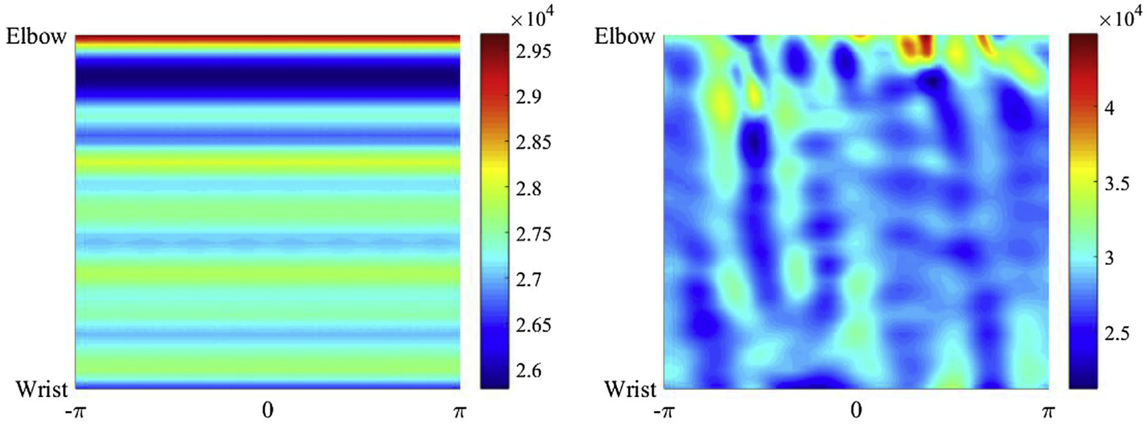

(a) Stress Skin Idealised (b) Stress Skin Actual

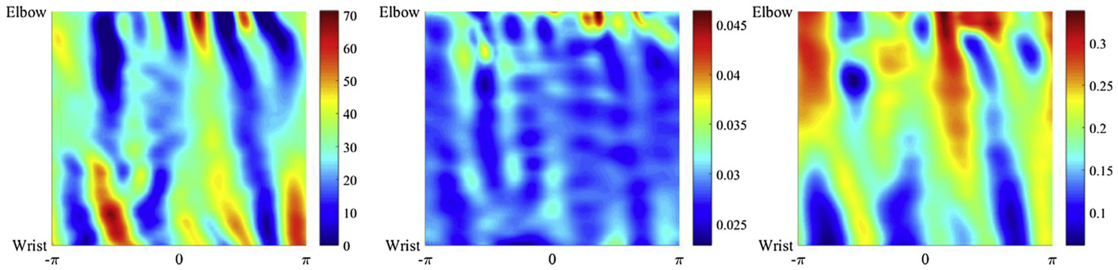

(c) Curvature (d) Strain skin (e) Strain fat

Fig. 4. Von Mises stress distributions (Pa) across the outer layer of skin for patient 11. (a) The homogeneous stress distribution at each cross-section of the idealised forearm. (b) The heterogeneous stress distribution on the actual forearm due to varying circumferential curvature. (c) The variation of curvature across the forearm of patient 11. Negative values were equated to zero, as to apply zero pressure based on Eq. (1). The strain distribution in the adipose tissue (d) had a higher correlation with curvature than that in the skin (e).

fibrotic and a higher garment pressure might be required. To study this effect P_g was increased for adipose tissue with a 4× higher stiffness (Fig. 8c and d). In line with the chosen material model, a very linear response was observed in the tissue stresses with the arm geometry determining the shape of the graph curves, whilst the P_g magnitude merely determined a constant offset in stress. Finally, the impact of a uniform adipose tissue thickness assumption on the circumferential stress distribution was investigated by perturbing the thickness of the adipose layer, $t_{adipose}$, as:

$$t_{adipose,new} = t_{adipose}(1 + 0.3sin(6\theta)) \tag{4}$$

Interestingly, Fig. 8(e) and (f) show that the stresses in the skin tissue are more sensitive to adipose tissue thickness variations than the stresses in the adipose tissues except near the elbow for the lower stiffness. The clinical relevance of this observation is currently still unkown.

4. Discussion

Compression therapy is considered to be a cornerstone of lymphoedemic management, and is widely employed to reduce swelling of lymphoedemic limbs (Mullings, 2012). Zaleska et al. showed experimentally that interstitial tissue fluid pressures are always lower than the applied external pressures using pneumatic compression devices (Zaleska et al., 2013). Therefore, the design and application of compression therapy is of great importance for the treatment of lymphoedema, but it is also relevant for the treatment of other pathological conditions such varicose veins and hypertrophic burn scars (Dubuis et al., 2012). The amount of pressure applied by compression garments, dictating the choice of garment class for each patient, is based on the assumption of circular limbs (Gaied et al., 2006; Macintyre, 2007). This study has illustrated the implications of such geometric assumptions and the errors introduced due to such assumptions were highlighted by simulating compression therapy using data-driven FE analysis.

Sub-bandage pressures, amongst other factors, dictate the efficacy of compression therapy (Brennan and Miller, 1998). For example, pressure values above 30 mmHg were found to be counterproductive for patients suffering from unilateral lymphoedema in their upper limbs (Partsch et al., 2011). Furthermore, the sub-bandage pressure distribution is heterogeneous in nature due to the non-circularity of human limbs. This implication would be significant in the treatment of lymphoedema, especially in the categorisation of medical garments based on circularity. Fig. 3 clearly shows the variability of the actual pressure across the forearm of a patient, $\widetilde{P}$, for an intended pressure, P_g, which is linearly diminishing from 2500 Pa at the wrist, to 2250 Pa at the elbow. The mean circumferential pressure at each cross-section of the forearm followed the intended pressure profile, but the variation in the actual pressure distribution for each cross-section was very high (due to non-circularity/curvature). To quantify the effect of these variations, all geometries were made circular whilst preserving the perimeter at each cross section, and the corresponding pressure distributions where compared to that corresponding to the true curvature of the forearm. The average RMSE across the cohort was just over a third of the maximum applied pressure. Such large variation occurred across the length of the forearm (Fig. 3), and

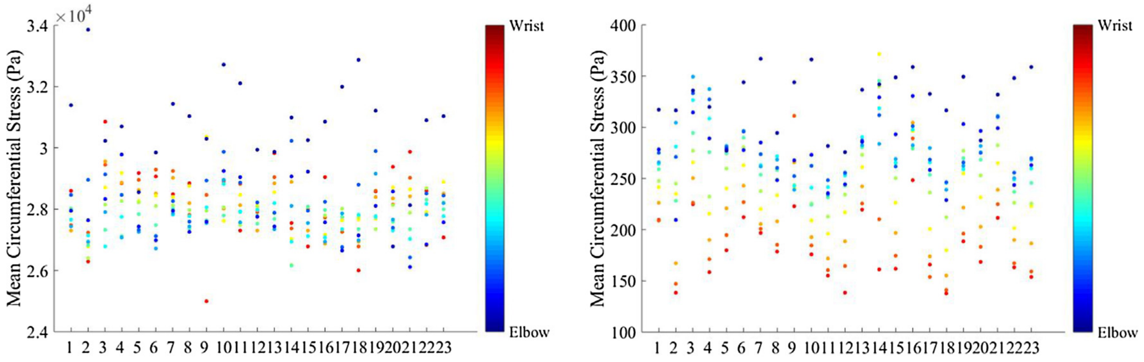

(a) Axial distribution of stress in outer skin layer (b) Axial distribution of stress in first layer of adipose tissue

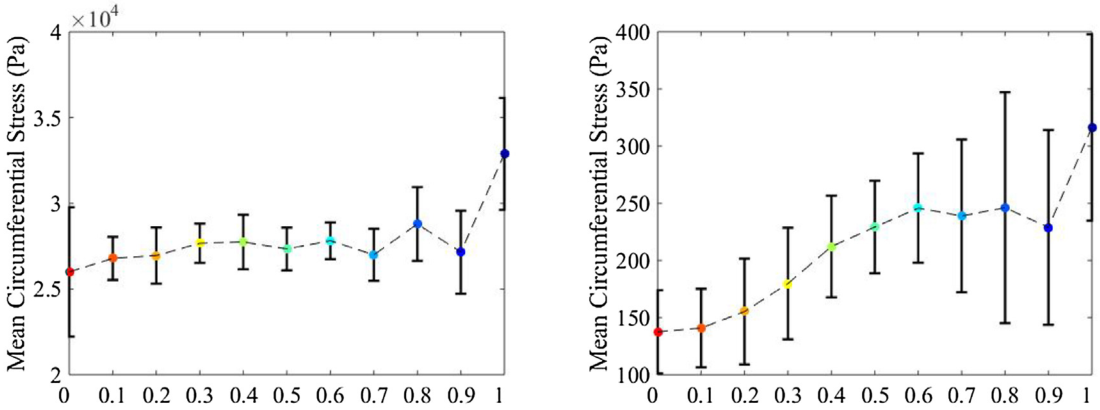

(c) Patient 18 skin stress distribution (d) Patient 18 adipose stress distribution

Fig. 5. (a) and (b) show the Von Mises stress distributions (Pa) across the forearms of all 23 patients. Each point within a column (patient) represents the mean circumferential stress at a given cross-section across the forearm. The colour code changes from red, indicating the position of the wrist, to blue, indicating the position of elbow. (a) Shows the mean circumferential stress values in the outer layer of skin tissue, while (b) shows the mean stress distribution in the outer layer adipose tissue. Notice how both soft tissues show different stress distributions and do not follow the intended axial pressure distribution, P_g, on the outer surface of skin. (c) and (d) illustrate the variation of stress across the forearm of patient 18. (For interpretation of the references to colour in this figure legend, the reader is referred to the web version of this article.)

should be taken into consideration when designing compression garments. The value for garment pressure, P_g, as reported by manufacturers, might deviate from the applied pressures, $\widetilde{P}$, for a given geometry, which might compromise treatment strategies employed by lymphoedema specialists. The 2D colourmaps of curvature (Fig. 4c) allow a visualisation of where the compression garments apply unnecessarily high, or critically low, pressures. These could inform lymphoedema specialists of areas receiving high/low sub-bandage pressures. Combining these with oedema maps, a diagnostic metric created in our previous study that visualises swelling across the arm (Karakashian et al., 2017), could allow for personalised treatment. Our tools for predicting and visualising sub-bandage pressures, based on 3D patient specific scans, are generated from a cost-effective scanning rig that could be easily accessible in clinical settings. It could also pave the way for creating new design/manufacturing methods to be used in the garment industry, especially when compared to FEA simulations of compression therapy as described next.

The initial and collecting lymphatics, which are situated in the skin and adipose layers respectively (Suami et al., 2012), are responsible for draining excess fluid based on several mechanical stimuli (Kunert et al., 2015; Scallan et al., 2010). In compression, the actual pressure distribution, $\widetilde{P}$, along with the behaviour of soft tissues in-vivo, determines the resultant subcutaneous pressure/stress distributions, which in return affect the lymphatics. When comparing the idealised soft tissue stresses/strains with that of the scan-based geometry, RMS errors were found high in the skin, yet relatively low in the adipose layers. From Fig. 4 it was noticed that in skin, stress distributions are more heterogeneous than in the adipose layers. Furthermore, the circular arms do not capture the circumferential movement/shearing of the soft tissues due to lacking actual convex and concave regions. The circumferential variation in curvature resulted in the movement and slight bulging of the soft tissues for the scan-based forearm models. This also explains having high stresses/strains in regions of negative curvature of the undeformed forearm (Fig. 4). Concave regions act as a focal point, where shear stresses are relatively large. This could provide an explanation as to why certain patients feel uncomfortable when wearing compression garments, which is relevant since comfort is closely linked to patient compliance in wearing garments.

Surprisingly, the resultant stress and strain distributions did not follow the negative axial gradient of the intended pressure distribution (Fig. 5). Most arms had a positive gradient in skin, while all arms had a positive gradient in the adipose layer. This phe-

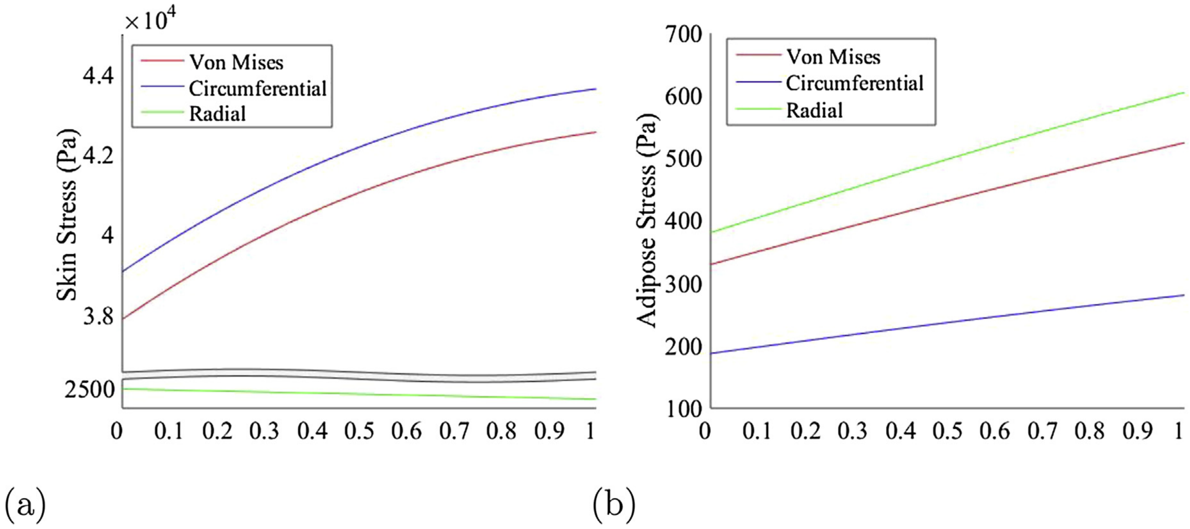

Fig. 6. Analytical solutions for stresses in the outer layer of skin (a) and adipose tissues (b) using thick-walled compound cylinder theory (see Appendix A). The cylinder had a tapering of 3 cm radius at the wrist, up to 4.5 cm at the elbow. Same FE material and boundary conditions were used. Overall stresses in skin and adipose tissues increased across the cylinder.

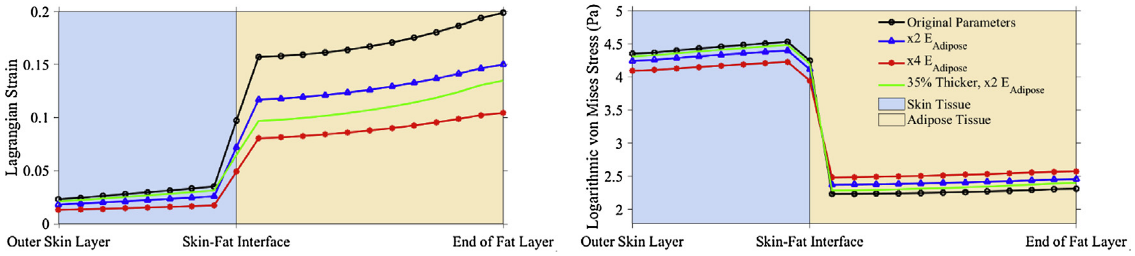

Fig. 7. Stress and strain variation with thickness and stiffness of adipose tissue. Results taken midway across the forearm of Patient 1, at $\theta = 0$.

nomenon was reproduced using the analytical formulations for thick-walled cylinders, and was noticed to be due to the following two factors:

1. having a tapered geometry, *and*
2. having two materials with highly different properties; skin and fat.

When both soft tissues were modelled as one material (results not shown), the stress/strains followed the outer negative gradient (point 2). The same behaviour was seen when modelling a perfect cylinder having two different layers; skin and fat (point 1). Fig. 6 illustrates that hoop/circumferential stresses cause this unusual behaviour, especially in skin, whilst the radial stresses were in balance with the outer applied pressure (Fig. 6a). As the skin is being compressed inwards from all directions, elements across the circumferential direction come closer together, increasing hoop stresses, and effectively increasing the total stresses (von Mises). All patients showed an increase of both radial and circumferential stresses in the adipose layer (Fig. 5b). Forearms that did not display this characteristic of positive gradient in the skin were larger in size relative to those that did. This suggests that the elements in the skin in these forearms are being ‘squeezed’ less in the circumferential direction, decreasing von Mises stresses. It was also noticed that the skin thickens when compressed, similar to a heart muscle wall thickening during contraction. The impact of this on lymphangions and initial lymphatics is unclear, but it could be hypothesized that the relatively small degree of stretching in the skin could open the initial lymphatics. Although the displacements were in the order of 10^{-4} m, they are two orders of magnitude larger than the size of initial lymphatics (Scallan et al., 2010). Also, lymphangions are sensitive to mechanical stimuli, such as shearing and compression (Kunert et al., 2015). Simulations carried by Kunert et al. show an increase in contraction of lymphangions when experiencing positive gradient of stresses (Kunert et al., 2015). Therefore, such positive gradients could stimulate the contraction of lymphangions and increase lymph drainage.

Although this work has elucidated some of the limitations of a Laplace law and has highlighted the issues relevant in compression therapy there are still additional challenges to overcome to make this framework more clinically relevant. The garment properties and garment geometries were not included in this work, but are likely to have a major impact on the stress and strain distribution across the arm tissues. There is variability in the material properties of garments from different manufacturers and the match/mismatch between arm shape and garment shape will have an impact on the pressure exerted onto an arm. In this work we chose to keep the “garment information” as constant, i.e. a fixed P_g, since this would add considerable complexity to the problem. However, this limits the viability of the current framework as clinical tool. Furthermore, the tissue properties will vary between patients and need to be measured (even if crude, but clinically obtainable) in order to establish the validity of our material models and coefficients, and to predict more patient-specific responses.

Hence, future work should incorporate the inclusion of patient-specific garment and tissue information and mapping FE/shape analysis results against patient outcomes. Furthermore there is an opportunity to couple the FE models with fluid transport models to study the effect of stress/strain distributions on blood and lymph transport. In particular, the subcutaneous pressures will influence the transmural pressures on lymphatic vessels, which will affect the pumping behaviour of lymphatic networks (Davis et al., 2012;

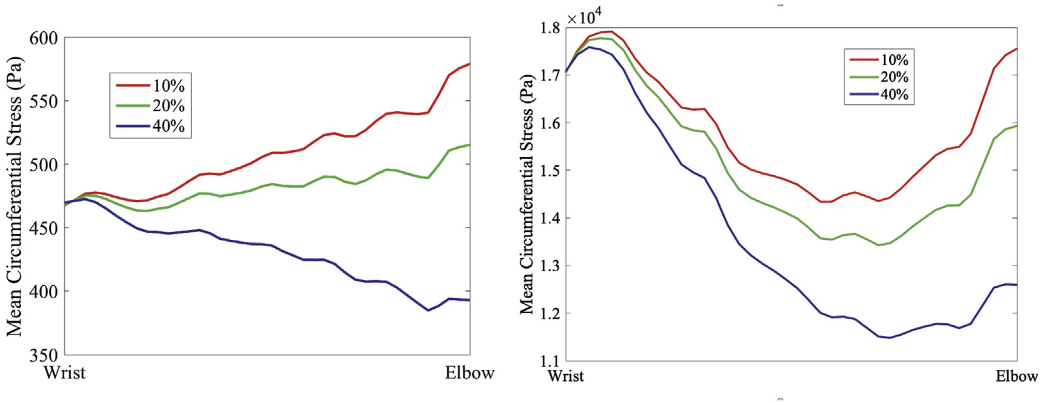

(a) Pressure gradients (adipose) (b) Pressure gradients (skin)

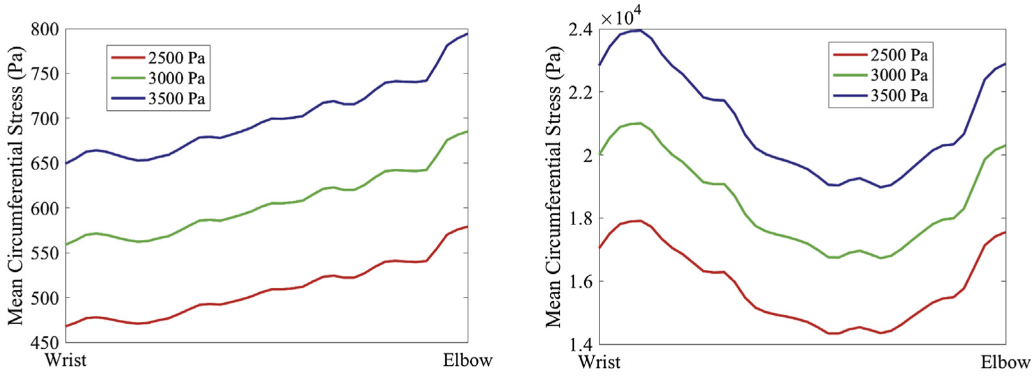

(c) Pressure magnitudes (adipose) (d) Pressure magnitudes (skin)

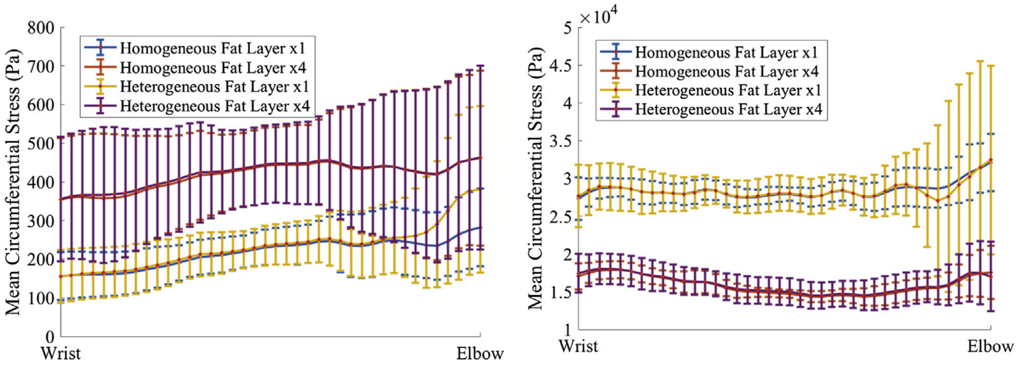

(e) Thickness variations (adipose) (f) Thickness variations (skin)

Fig. 8. Varying axial distributions of stress for patient 11 to study the sensitivity of our models to some parameters. In the upper two graphs (a,b) three different gradients for the garment pressure were introduced for an arm with 4× higher stiffness. In the middle two graphs (c,d) the magnitude of the garment pressure was increased for an arm with a 4× higher stiffness. In the lower two graphs (e,f) models with a uniform thickness of the adipose layer were compared against a varying thickness (circumferentially). The standard deviations of the stresses are given for each cross-section.

Scallan et al., 2016). A coupling between our work and models as proposed in Bertram et al. (2017),Caulk et al. (2017) would be very well-suited to study the longer term transient effects of compression treatment. Figs. 8a, and b further demonstrate the need for such analyses. Increasing the drop of P_g across the arm, eventually caused average von Mises stresses to follow the outer gradient of applied pressure (Fig. 8b). The impact of such outcome is more prominent in transient clinical scenarios, where the flow of interstitial fluid would be triggered under a negative pressure gradient (distal to proximal). At the same time, these results support the conclusion of literature that higher mean P_g across the arm may not always be beneficial (Partsch et al., 2011).

In conclusion, this study has provided new insight on the variability of sub-garment and (sub)-cutaneous stress/strain fields in compression therapy. It was illustrated that 3D scanning could provide lymphoedema clinics with a novel and non-invasive source of patient information that has the potential to aid compression therapy treatment planning.

Author contributions

KK and RvL performed the FEA. CP collected the patient data. RvL and CP designed the study. All authors read and approved the final manuscript.

Conflict of interest

The authors report no conflict of interest.

Acknowledgements

No acknowledgements.

Appendix A

A.1. Geometry mapping procedure

First, a 2D mesh was created in MATLAB having different material layers of skin, adipose and muscle as concentric circles, which was then extruded uniformly with the assumption that the soft tissues will not vary in size along the plane of extrusion (Fig. 1). Meshing the 2D cross section first and then extruding it allowed to have structured elements within the soft tissues, which cylindrical coordinates may easily express for post-processing. Second, to find the points onto which the volumetric mesh must be projected to, the segmented scan of forearm was aligned with the volumetric mesh such that their principal axes were aligned to one another. Then, a transformation from Cartesian (x_i, y_i, z_i) to cylindrical coordinates (r_i, θ_i, z_i) was performed for each i-th node (vertex) in the triangulation (see Appendix A). The outer layer of the volumetric mesh, N_θ (circumferential nodes) by N_z (axial nodes), was then defined with coordinates $(\hat{\theta}_j, \hat{z}_j)$. Note that $\pi < \hat{\theta}_j \leqslant \pi$ and $0 \leqslant \hat{z}_j \leqslant L$ where L is the length of the forearm and $\hat{z}_j = 0$ at the wrist. For every node $(\hat{\theta}_j, \hat{z}_j)$ a triangle Tr_j was found and the barycentric coordinates for the outer grid nodes within Tr_j were saved (see also Fig. A.9 in the Appendix A) (Karakashian et al., 2017). The volumetric mesh was then radially displaced in

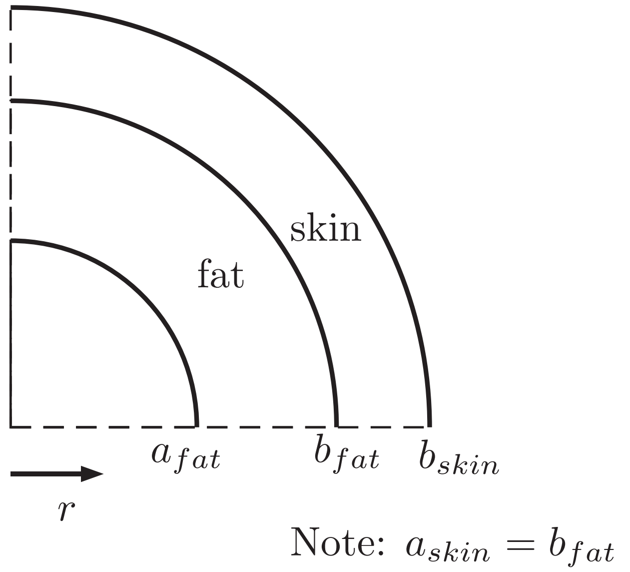

Fig. A.10. Visualisation of the thick-walled cylinder theory. The boundary conditions at the different interfaces are: $u_{fat}(r = a_{fat}) = 0, u_{fat}(r = b_{fat}) = u_{skin}(r = a_{skin})$ and $p_o(r = b_{skin}) = P_g$.

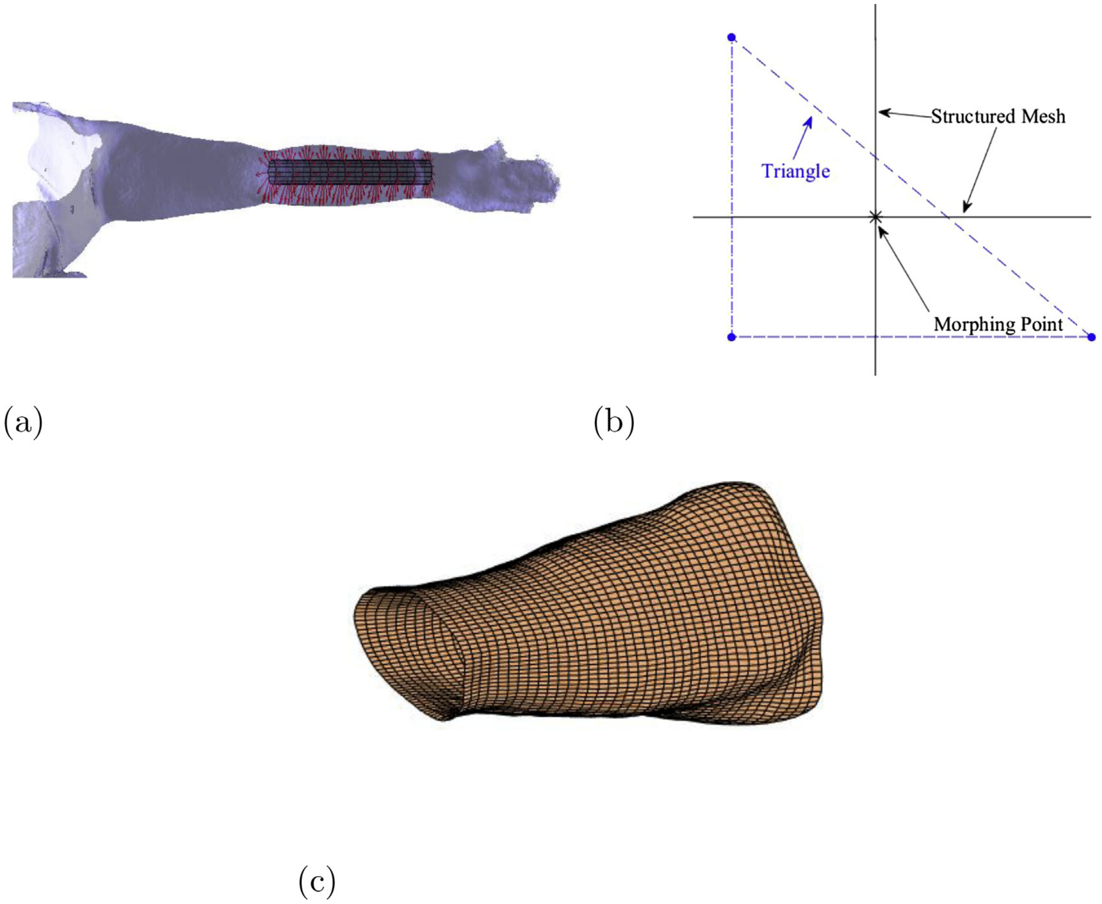

Fig. A.9. Illustration of the mapping procedure performed. (a) The outer surface of the structured template FE mesh (grey) aligned with forearm in STL format (blue/purple). The red arrows depict the radial positions the FE nodes must be morphed to. (b) The projection onto the $\theta - z$ plane of a node from the FE mesh surface (black) overlaying the triangular surface mesh (STL). (c) The morphed FE mesh that can be used for calculations. (For interpretation of the references to colour in this figure legend, the reader is referred to the web version of this article.)

MATLAB to these morphing positions, maintaining the uniform pre-defined thickness for all soft tissues. It should be noted that the muscle tissue was removed, as explained in the following section, since its effect on (sub)cutaneous stress and strain distributions was found to be minimal (Fig. 2). After morphing the structured mesh, a low pass filter was used to smooth the geometry (Dubuis et al., 2012).

Fig. A.9a shows a segmented arm de-cluttered from patient's body and surrounding clinical environment. The forearm, visualised here with the rest of the arm, is first aligned with FE volumetric mesh. The outer nodes of the FE mesh are then overlaid on top of the triangular surface mesh, i.e. converted into cylindrical coordinates to assign a triangle for each of these nodes using barycentric coordinate system (Fig. A.9b). These 'morphing' points can be converted from barycentric into Cartesian coordinates to get a morphed structured mesh (Fig. A.9c). The radial values of the morphed mesh were then used to radially displace all inner nodes of the volumetric mesh as explained in the Methodology Section 2.3. The geometries of all the arms considered in this work are shown in Fig. A.11.

A.2. Neo-Hookean model

The strain energy potential (U) for finite strains is as follows:

$$U = C_{10}\left(\bar{I} - 3\right) + \frac{1}{D_1}\left(J_{el} - 1\right)^2, \tag{A.1}$$

where $\overline{I_1}$ is the first deviatoric strain invariant and J_{el} is the elastic volume ratio. C_{10} and D_1 are material parameters given by:

$$C_{10} = \frac{G_0}{2}, \tag{A.2}$$

$$D_1 = \frac{3(1 - 2\nu)}{G_0(1 + \nu)}. \tag{A.3}$$

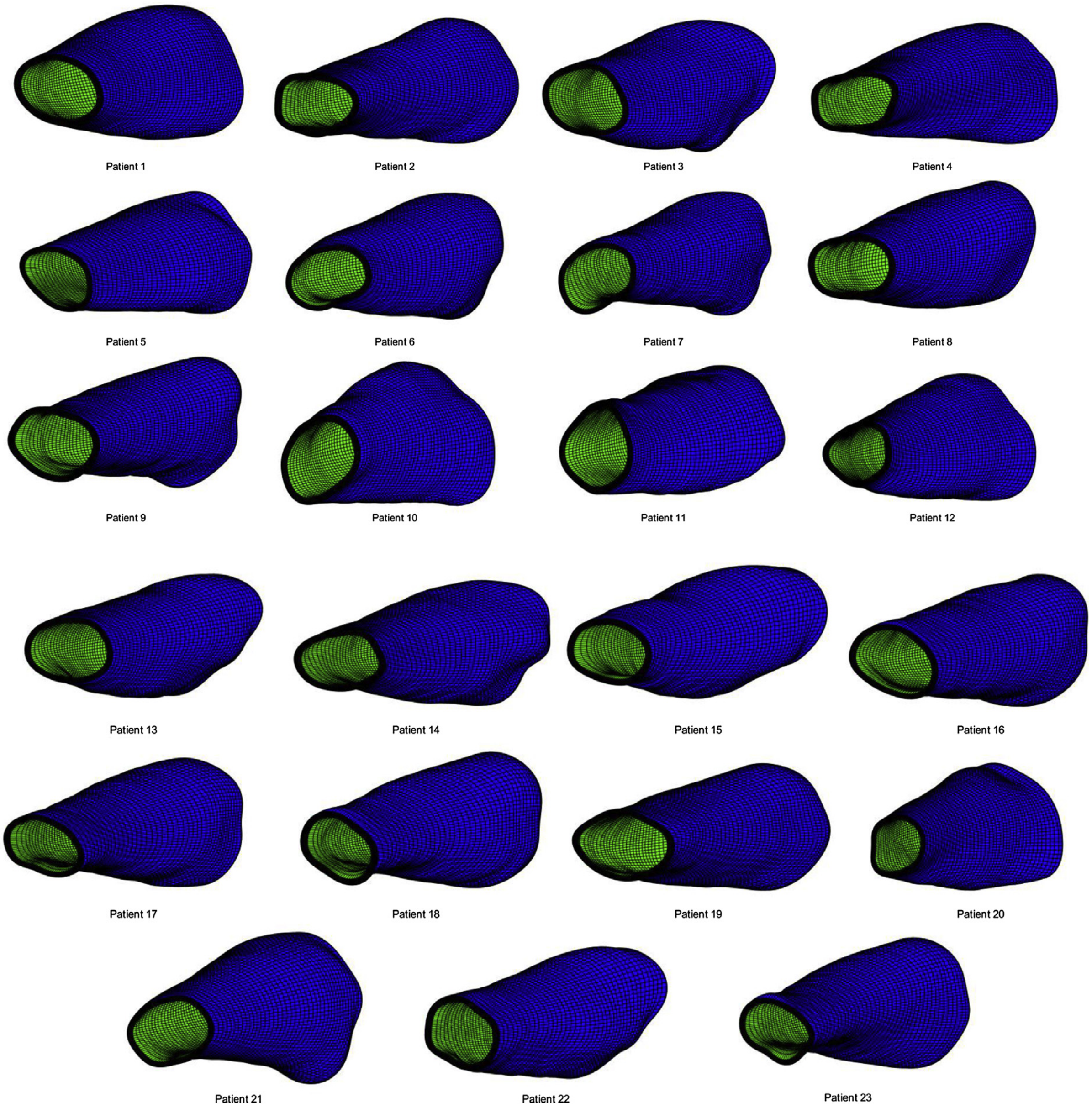

Patient 1 Patient 2 Patient 3 Patient 4

Patient 5 Patient 6 Patient 7 Patient 8

Patient 9 Patient 10 Patient 11 Patient 12

Patient 13 Patient 14 Patient 15 Patient 16

Patient 17 Patient 18 Patient 19 Patient 20

Patient 21 Patient 22 Patient 23

Fig. A.11. Visualisation of all the arm geometries.

G_0 is the shear modulus and ν is Poisson's ratio. The shear modulus in return can be rewritten in terms of Young's modulus E and Poisson's ratio,

$$G_0 = \frac{E}{2(1+\nu)}, \tag{A.4}$$

requiring only to define the values of Young's moduli and Poisson's ratio of each soft tissue.

A.3. Elastic thick-walled cylinders

The application of uniform pressure on the external and/or internal faces to an elastic thick-walled cylinder, results in symmetrical deformations about the axial z-axis. In plane stress conditions, assuming the cylinder to be unconstrained from both sides ($\sigma_z = 0$), the circumferential (σ_θ) and radial stresses (σ_r) at each cross-section, along with radial displacements (u) are given as Ugural and Fenster (1995),

$$\sigma_r(r) = \frac{a^2 p_i - b^2 p_o}{b^2 - a^2} - \frac{(p_i - p_o) a^2 b^2}{\left(b^2 - a^2\right) r^2} \tag{A.5}$$

$$\sigma_\theta(r) = \frac{a^2 p_i - b^2 p_o}{b^2 - a^2} + \frac{(p_i - p_o) a^2 b^2}{\left(b^2 - a^2\right) r^2} \tag{A.6}$$

$$u(r) = \frac{1-\nu}{E} \frac{\left(a^2 p_i - b^2 p_o\right) r}{b^2 - a^2} + \frac{1+\nu}{E} \frac{(p_i - p_o) a^2 b^2}{\left(b^2 - a^2\right) r} \tag{A.7}$$

where r is the radial position within a cross-section, a is the inner radius of cylinder, b is the outer radius of cylinder, p_o is the outer pressure $p(r = b)$, p_i is the inner pressure $p(r = a)$, ν is the Poisson's ratio and E is the Young's modulus.

In this study, the modelled geometries could be simplified into tapered cylinders composed of two layers (compound cylinders) as illustrated in Fig. A.10. The above three parameters for a compound cylinder could be found by coupling both layers using the displacement Eq. (A.7) i.e. the displacements of both skin and fat at the skin-fat interface are equal to one another. Also, due to the fixed boundary conditions at the muscle-fat interface, the displacement at the inner wall of the compound cylinder equals to zero i.e. $p_i|_{r=a_{fat}} \neq 0$. This introduces a system of two equations with two unknown variables to be solved for; $p_i|_{r=a_{fat}}$ and the developed pressure at the skin-fat interface, $p_t = p_o|_{r=b_{fat}} = p_i|_{r=a_{skin}}$. These could be algebraically solved for, and the formulation for the radial displacement of skin is shown below.

$$u_{skin} = \frac{1-\nu_{skin}}{E_{skin}} \frac{\left(a^2 p_t - b^2 p_{o\_skin}\right) r}{b^2 - a^2} + \frac{1+\nu_{skin}}{E_{skin}} \frac{(p_t - p_{o\_skin}) a^2 b^2}{\left(b^2 - a^2\right) r} \tag{A.8}$$

where $p_{o\_skin} = P_g$.

References

Bertram, C.D., Macaskill, C., Davis, M.J., Moore Jr., J.E., 2017. Valve-related modes of pump failure in collecting lymphatics: numerical and experimental investigation. Biomech. Model. Mechanobiol. 16, 1987–2003.

Brennan, M.J., Miller, L.T., 1998. Overview of treatment options and review of the current role and use of compression garments, intermittent pumps, and exercise in the management of lymphedema. Cancer 83 (12), 2821–2827.

Buffa, R., Mereu, E., Lussu, P., Succa, V., Pisanu, T., Buffa, F., Marini, E., 2015. A new, effective and low-cost three-dimensional approach for the estimation of upper-limb volume. Sensors 15 (6), 12342–12357.

Caulk, A.W., Dixon, J.B., Gleason, R.L., 2017. A lumped parameter model of mechanically-mediated acute and long-term adaptations of contractility and geometry in lymphatics for characterization of lymphedema. Biomech. Model. Mechanobiol. 15 (6), 1601–1618.

Davis, M.J., Rahbar, E., Gashev, A.A., Zawieja, D.C., Moore Jr, J.E., 2012. Determinants of valve gating in collecting lymphatic vessels from rat mesentery. Am. J. Phys. - Heart and Circ. Phys. 2011;301 (1), :H48–:H60.

Dubuis, L., Avril, S., Debayle, J., Badel, P., 2012. Identification of the material parameters of soft tissues in the compressed leg. Comput. Method. Biomech. Biomed. Eng. 15 (1), 3–11.

Frauziols, F., Molimard, J., Navarro, L., Badel, P., Viallon, M., Testa, R., Avril, S., 2015. Prediction of the biomechanical effects of compression therapy by finite element modeling and ultrasound elastography. IEEE Trans. Biomed. Eng. 62 (4), 1011–1019.

Freutel, M., Schmidt, H., Dürselen, L., Ignatius, A., Galbusera, F., 2014. Finite element modeling of soft tissues: material models, tissue interaction and challenges. Clin. Biomech. 29 (4), 363–372.

Gaied, I., Drapier, S., Lun, B., 2006. Experimental assessment and analytical 2D predictions of the stocking pressures induced on a model leg by Medical Compressive Stockings. J. Biomech. 39 (16), 3017–3025.

Geerligs, M., van Breemen, L., Peters, G., Ackermans, P., Baaijens, F., Oomens, C., 2011. In vitro indentation to determine the mechanical properties of epidermis. J. Biomech. 44 (6), 1176–1181.

Huang, T.-W., Tseng, S.-H., Lin, C.-C., Bai, C.-H., Chen, C.-S., Hung, C.-S., Wu, C.-H., Tam, K.-W., 2013. Effects of manual lymphatic drainage on breast cancer-related lymphedema: a systematic review and meta-analysis of randomized controlled trials. World J. Surg. Oncol. 11 (1), 15.

Iivarinen, J.T., Korhonen, R.K., Julkunen, P., Jurvelin, J.S., 2011. Experimental and computational analysis of soft tissue stiffness in forearm using a manual indentation device. Med. Eng. Phys. 33 (10), 1245–1253.

Iivarinen, J.T., Korhonen, R.K., Julkunen, P., Jurvelin, J.S., 2013. Experimental and computational analysis of soft tissue mechanical response under negative pressure in forearm. Skin Res. Technol. 19 (1), 356–365.

Iivarinen, J.T., Korhonen, R.K., Jurvelin, J.S., 2016. Modeling of interstitial fluid movement in soft tissue under negative pressure relevance to treatment of tissue swelling. Comput. Method. Biomech. Biomed. Eng. 19 (10), 1089–1098.

Kaczmarek, M., Olszewski, W.L., Nowak, J., Nowak, B., Zaleska, M., 2013. Simulations of creep in lymphedematous tissue under the load of the modified harpenden caliper tip. J. Health Sci. 3 (13), 259–266.

Karakashian et al., 2018. Investigation of Shape with Patients Suffering from Unilateral Lymphoedema. Annals of Biomedical Engineering 46 (1).

Krimmel, G., 2009. The construction and classification of compression garments. In: Template for Practice: Compression hosiery in upper body lymphoedema. HealthComm UK Ltd, Aberdeen, p. 5.

Kunert, C., Baish, J.W., Liao, S., Padera, T.P., Munn, L.L., 2015. Mechanobiological oscillators control lymph flow. Proc. Natl. Acad. Sci. United States of America 112 (35), 10938–10943.

Lawenda, B.D., Mondry, T.E., Johnstone, P.A.S., 2009. Lymphedema: a primer on the identification and management of a chronic condition in oncologic treatment. CA Can. J. Clin. 59 (1), 8–24.

Linder-Ganz, E., Gefen, A., 2004. Mechanical compression-induced pressure sores in rat hindlimb: muscle stiffness, histology, and computational models. J. Appl. Physiol. 96 (6), 2034–2049.

Macintyre, L., 2007. Designing pressure garments capable of exerting specific pressures on limbs. Burns 33 (5), 579–586.

Mortimer, P., Levick, J., 2004. Chronic peripheral oedema: the critical role of the lymphatic system. Clin. Med. 4 (5), 448–453.

Mullings, J., 2012. Juxta-Fit compression garments in lymphoedema management. Brit. J. Commun. Nurs. 17 (10), S32–S37.

Olszewski, W.L., Ambujam, P.J.G., Zaleska, M., Cakala, M., 2009. Where do lymph and tissue fluid accumulate in lymphedema of the lower limbs caused by obliteration of lymphatic collectors? Lymphology 42 (3), 105–111.

Palfreyman, S.J., Michaels, J.A., 2009. A systematic review of compression hosiery for uncomplicated varicose veins. Phlebology 24 (1), 13–33.

Partsch, H., Damstra, R.J., Mosti, G., 2011. Dose finding for an optimal compression pressure to reduce chronic edema of the extremities. Int. Angiol.: A J. Int. Union Angiol. 30 (6), 527–533.

Partsch, H., Flour, M., Smith, P.C., 2008. Indications for compression therapy in venous and lymphatic disease consensus based on experimental data and scientific evidence. Under the auspices of the IUP. Int. Angiol.: A J. Int. Union Angiol. 27 (3), 193–219. International Compression Club.

Pawlaczyk, M., Lelonkiewicz, M., Wieczorowski, M., 2013. Age-dependent biomechanical properties of the skin. Postepy dermatologii i alergologii 30 (5), 302–306.

Pellicer, J., Garcia-Morales, V., Hernandez, M., 2000. On the demonstration of the Young-Laplace equation in introductory physics courses. Phys. Educ. 35 (2), 126–129.

Piller, N., 2012. Getting the pressure right: how do we know? J. Lymphoedema 7 (2), 6.

Scallan, J., Huxley, V.H., Korthuis, R.J., 2010. The Lymphatic Vasculature. Morgan & Claypool Life Sciences. San Rafael. Ch. Ch. 3.1–3.2..

Scallan, J.P., Zawieja, S.D., Castorena Gonzalez, J.A., Davis, M.J., 2016. Lymphatic pumping: mechanics, mechanisms and malfunction. J. Phys. 594 (20), 5749–5768.

Suami, H., Chang, D., Skoracki, R., Yamada, K., Kimata, Y., 2012. Using indocyanine green fluorescent lymphography to demonstrate lymphatic architecture. J. Lymphoedema 7 (2), 25–29.

Tran, H.V., Charleux, F., Rachik, M., Ehrlacher, A., Ho Ba Tho, M.C., 2007. In vivo characterization of the mechanical properties of human skin derived from MRI and indentation techniques. Comput. Methods Biomech. Biomed. Eng. 10 (6), 401–407.

Ugural, A.C., Fenster, S.K., 1995. Advanced Strength and Applied Elasticity. Prentice-Hall. Chapter 8, 328–333.

Zaleska, M., Olszewski, W.L., Jain, P., Gogia, S., Rekha, A., Mishra, S., Durlik, M., 2013. Pressures and timing of intermittent pneumatic compression devices for efficient tissue fluid and lymph flow in limbs with lymphedema. Lymphatic Res. Biol. 11 (4), 227–232.